ACS NANO

www.acsnano.org

ARTICLE

Modular Assembly of MXene Frameworks for Noninvasive Disease Diagnosis via Urinary Volatiles

Xuyin Ding, Yecheng Zhang, Yue Zhang, Xufa Ding, Hanxin Zhang, Tian Cao, Zhi-bei Qu, Jing Ren, Lei Li, Zhijun Guo, Feng Xu, Qi-Xian Wang, Xing Wu, Guoyue Shi, Hossam Haick,* and Min Zhang*

Cite This: *ACS Nano* 2022, 16, 17376–17388

Read Online

ACCESS | Metrics & More | Article Recommendations | Supporting Information

ABSTRACT: Volatile organic compounds (VOCs) in urine are valuable biomarkers for noninvasive disease diagnosis. Herein, a facile coordination-driven modular assembly strategy is used for developing a library of gas-sensing materials based on porous MXene frameworks (MFs). Taking advantage of modules with diverse composition and tunable structure, our MFs-based library can provide more choices to satisfy gas-sensing demands. Meanwhile, the laser-induced graphene interdigital electrodes array and microchamber are laser-engraved for the assembly of a microchamber-hosted MF (MHMF) e-nose. Our MHMF e-nose possesses high-discriminative pattern recognition for simultaneous sensing and distinguishing of complex VOCs. Furthermore, with the MHMF e-nose being a plug-and-play module, a point-of-care testing (POCT) platform is modularly assembled for wireless and real-time monitoring of urinary volatiles from clinical samples. By virtue of machine learning, our POCT platform achieves noninvasive diagnosis of multiple diseases with a high accuracy of 91.7%, providing a favorable opportunity for early disease diagnosis, disease course monitoring, and relevant research.

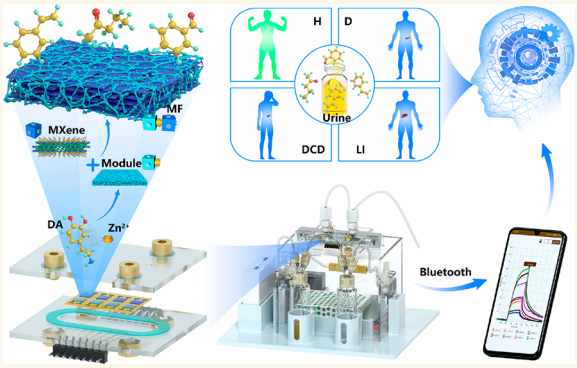

KEYWORDS: *MXene frameworks, e-nose, urinary volatiles, machine learning, noninvasive disease diagnosis*

INTRODUCTION

Urine contains the final metabolic products filtered by the kidney after metabolism.[1] Urinary metabolites can directly reflect the pathological and physiological conditions of the body, acting as an ideal source of disease markers, and urinary metabolites can be useful for the noninvasive study of body metabolism.[2−4] Current research on urinary metabolites mainly focuses on the detection of soluble metabolites (e.g., proteins) and volatile organic compounds (VOCs) in urine. Most of the traditional techniques used are off-line and rely on large and expensive instruments such as gas chromatography-mass spectrometry (GC-MS), requiring steps of specific sample pretreatments. Although these techniques have produced great achievements, they are inadequate for direct, fast, and real-time detection and seldom meet the requirements of point-of-care testing (POCT).[5] Compared with GC-MS, electronic noses (e-noses) that mimic human olfaction in the recognition of different VOCs are cheaper, faster, and more suitable for portability.[6−9] Therefore, it is highly useful to create simple, cost-effective, and high-performance e-noses for monitoring of urinary metabolites (especially urinary VOCs) and further research a POCT platform toward noninvasive disease diagnosis.

The core of e-noses is the sensing material. The metal oxide semiconductor (MOS) is one of the common sensing materials used.[10] MOS-based e-noses usually work in high temperatures (>100 °C) during the sensing process,[11] which may result in high-power consumption or induce safety issues upon exposure to explosive VOCs. E-noses using other sensing materials (e.g., conducting polymers,[12] black phosphorene,[13] etc.) may suffer from either poor stability or a low sensitivity, thus limiting their practical application. It is important to seek sensing materials or optimize structures for building high-performance e-noses.[14−16]

Received: August 18, 2022
Accepted: October 10, 2022
Published: October 13, 2022

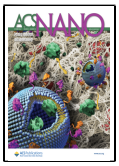

https://doi.org/10.1021/acsnano.2c08266
ACS Nano 2022, 16, 17376−17388

Scheme 1. Modular Assembly of MXene Frameworks for Noninvasive Disease Diagnosis via Urinary Volatiles[a]

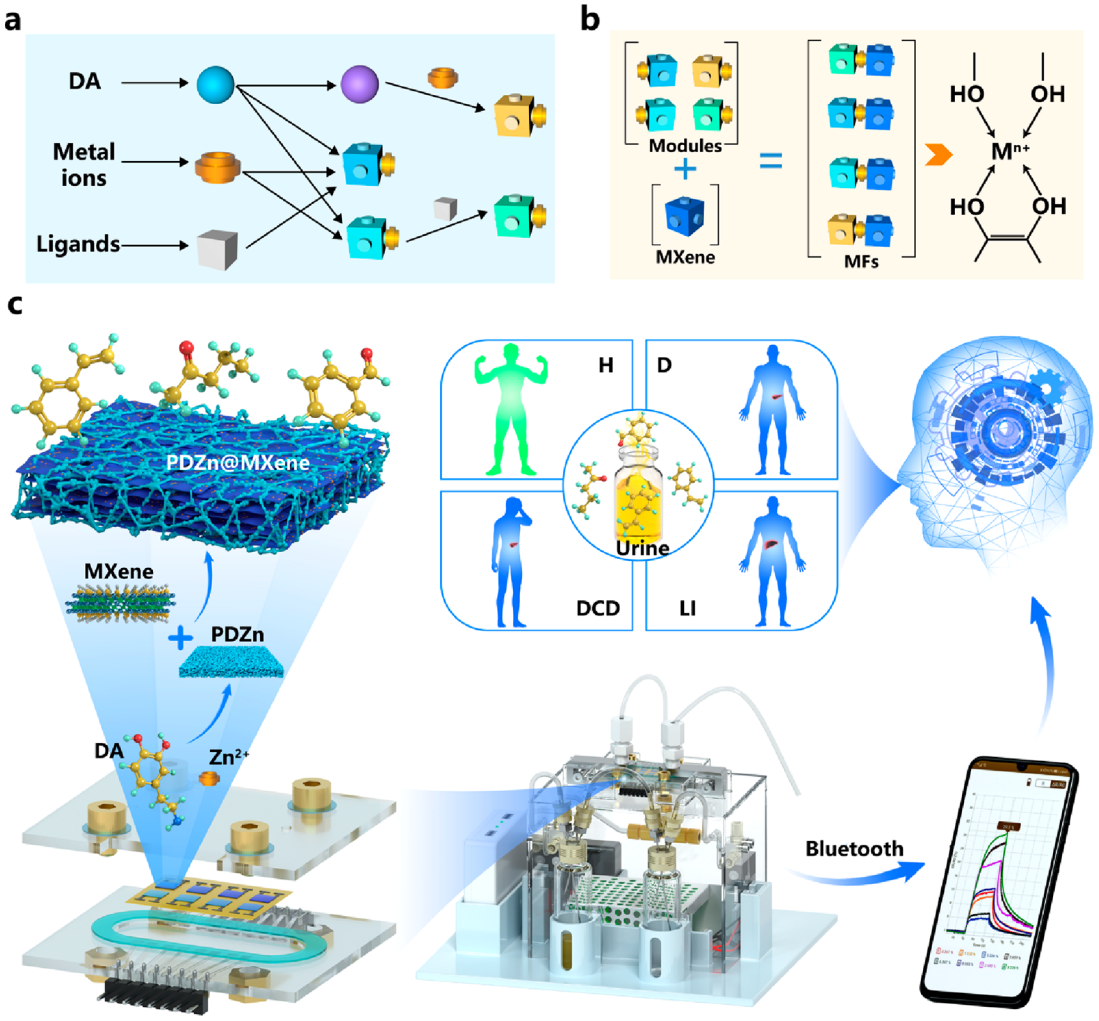

[a](a) Synthesis of versatile modules based on dopamine, metal ions, and ligands by metal ion-doped, ligand-engineered and sequence-regulated strategies. (b) Coordination-driven modular assembly of porous MFs with the selection of modules and MXene, including the interaction of linkage between modules and MXene. (c) Construction of the MHMF e-nose and a portable POCT platform for monitoring urinary VOCs towards noninvasive disease diagnosis by ML.

The porous gas-sensing materials are beneficial in expanding the active surface and the acceleration of gas diffusion,[16−19] boosting gas-sensing performance. Moreover, the development of gas-sensing materials that can provide multiple interactions (e.g., hydrogen bonds, coordination bonds and $\pi-\pi$ conjugates) with VOCs can improve their capability for complex VOCs recognition.[20] Metal coordination-driven self-assembly of inorganic or organic molecules is common in nature,[21−23] which can endow some desirable properties. For example, metal ions cross-linked with biomolecules and simultaneously incorporated in some ligands can produce multifunctional and structure-tuned nanohybrids.[24−27] Featuring abundant raw materials, diverse interactions, and structural tunability (such as a gel-like percolating nanoscale network), these nanohybrids are potential gas-sensing materials. However, the poor or lacking conductivity for most of these nanohybrids limits their utilization as chemiresistive gas-sensing materials. MXenes, a class of two-dimensional (2D) transition-metal carbides and nitrides, have attracted recent attention as gas-sensing materials, due to their superior properties, such as rich terminal functional groups facilitating to functional modification and excellent metallic conductivity providing high electrical conductivity.[28,29] Some investigations of MXene-based sensors are aimed at VOCs sensing.[30−32] To date, there are few reports on MXene frameworks (MFs) via coordination-driven modular assembly for high-performance sensing of complex VOCs, especially for clinical trials.

Ideal e-noses are expensive but durable and reusable or inexpensive to make and disposable.[33] Because of the space distribution of gas molecules in a measurement chamber effecting the performance of e-noses,[34] the design of the chambers is essential. Additionally, configuration of a portable and cost-effective sensing module is the pivotal challenge that needs to be solved to gain clinical applications for high-performance VOCs, especially the unveiling of the chamber-sensor-on-a-chip. Researchers recently have reported the laser-engraved method for micro/nano processing,[35−37] which is easy, low cost, and design flexible. Thus, the above demands regarding the chamber-sensor-on-a-chip are expected to be realized with the laser-engraved technique.

In this work, a portable POCT platform with an integrated e-nose was constructed for wireless and real-time monitoring of

https://doi.org/10.1021/acsnano.2c08266
ACS Nano 2022, 16, 17376−17388

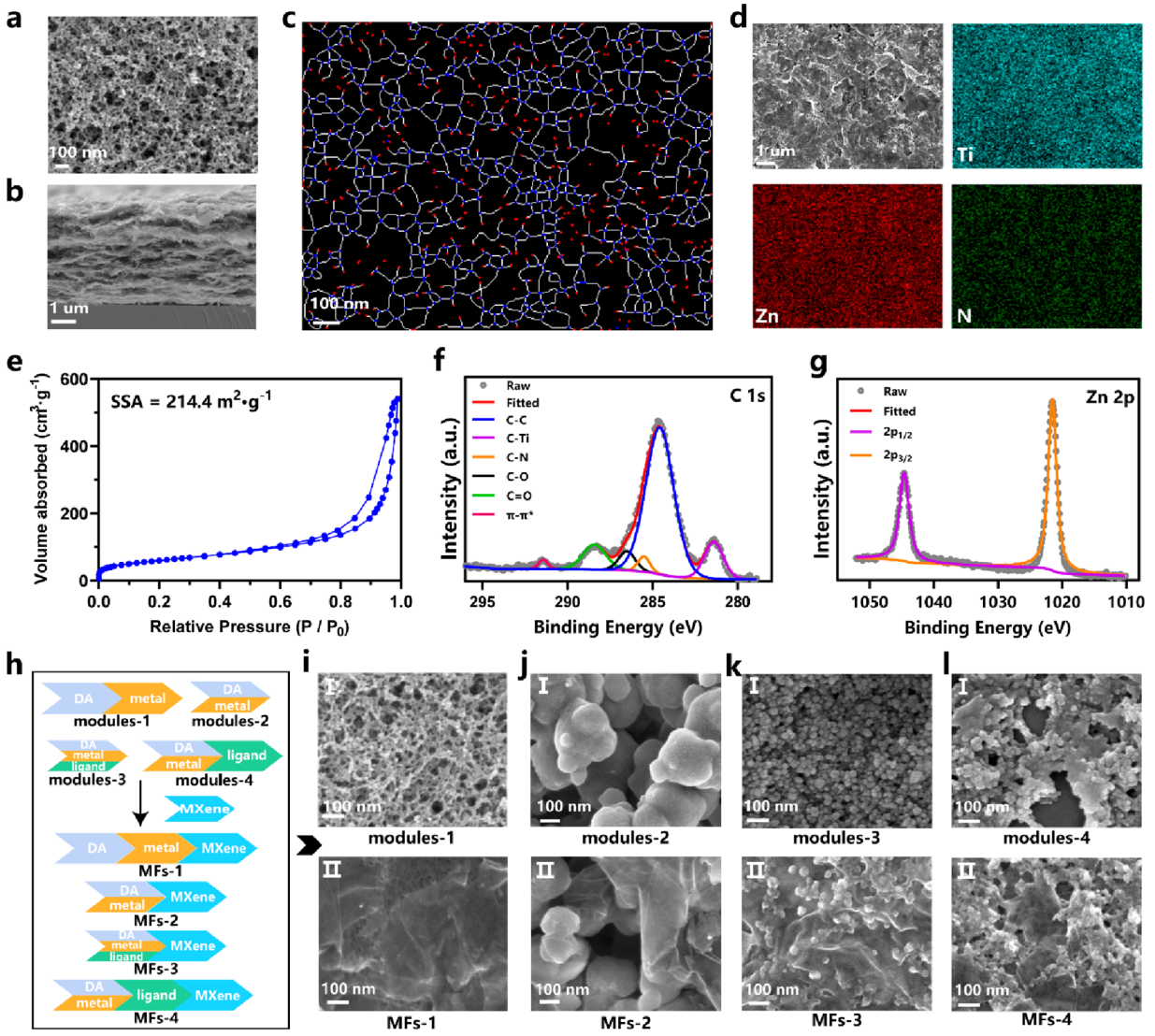

Figure 1. Characterizations of porous MFs. (a) SEM image of PDZn-3 h. (b) Cross-sectional SEM image of PDZn@MXene. (c) "Skeleton" image extracted from the binary version of SEM image of PDZn-3 h by GT analysis. Branch points are identified with blue dots, end points are identified with red dots, and edges are identified with white lines. (d) Top-view SEM image and EDS mapping analysis of Ti, Zn, and N distribution in PDZn@MXene. (e) N_2 adsorption−desorption isotherm of PDZn@MXene. XPS spectrum of PDZn@MXene in (f) C 1s region and (g) Zn 2p region. (h) Illustration of coordination-driven modular assembly of porous MFs from DA, metal ions, ligands, and MXene. SEM images of (i−l) in I for PD@Zn (modules-1), PDCa (modules-2), PDZnOA (modules-3), and PDZn@Lys (modules-4) and in II for PD@Zn@MXene (MFs-1), PDCa@MXene (MFs-2), PDZnOA@MXene (MFs-3), and PDZn@Lys@MXene (MFs-4), respectively.

urinary VOCs toward noninvasive disease diagnosis, where porous MFs were chemically tuned to become gas-sensing materials via the coordination-driven modular assembly and hosted in a compact laser-engraved microchamber (Scheme 1). As a proof-of-concept design, a typical MF (PDZn@MXene) was prepared by the incorporation of MXene nanosheets with a percolating nanoscale network of Zn^{2+}-bridged polydopamine (PDZn) in a coordination-driven assembly strategy. We then demonstrated that changes of metal moieties, chemical ligands, and their reaction sequences can build modules with different compositions, structures, and functionalities, producing a library of chemically modified MFs with well-defined and tailored properties. The as-prepared MFs can function as a pool of sensing materials with divergent sensing responses toward various VOCs. With the aid of laser-engraved technology, we fabricated a 2 × 4 array of laser-induced graphene interdigital electrodes (LIGIE) to load 8 kinds of MFs for assembling the VOCs' sensor array. To save space and increase cost-effectiveness, the sensor array was then fixed into a laser-engraved microchamber for the modular assembly of a microchamber-hosted MFs (MHMF) e-nose with the size 5.44 cm (L) × 4.50 cm (W) × 0.42 cm (H). Our MHMF e-nose was utilized as a versatile chamber-sensor-on-a-chip for real-time recording of the MFs' chemiresistive responses to VOCs. Owing to both the porous structure of the MFs and the utility of the microchamber, the resulting MHMF e-nose showed fast response/recovery (<1 min), good reversibility, and improved sensing capabilities for various VOCs. Our MHMF e-nose, as a cross-reactive sensory device, can provide high-discriminative competence in the simultaneous sensing and pattern recognition of complex VOCs. Taking advantage of the MHMF e-nose as a sensing module, we have further modularly assembled a portable POCT system for "smelling" urinary volatiles from clinical samples targeting health (H), patients with diabetic comorbid

https://doi.org/10.1021/acsnano.2c08266
ACS Nano 2022, 16, 17376−17388

depression (DCD), diabetes (D), and liver impairment (LI). On the basis of urinary volatiles, our POCT platform has successfully implemented noninvasive disease diagnosis with an accuracy of 91.7% when assisted by machine learning (ML).

RESULTS AND DISCUSSION

Coordination-Driven Modular Assembly of Porous MXene Frameworks. Multilayer $Ti_3C_2T_x$ MXene (m-MXene) was obtained from the selective etching of Al from Ti_3AlC_2 (MAX) by LiF/HCl. Then MXene nanosheets were prepared from the freeze−thaw assisted exfoliation of m-MXene.[38] In a typical synthesis, the 104 peak of MAX at 38.9° vanished in $Ti_3C_2T_x$ (MXene), proving the successful removal of Al,[39] and the 002 peak was shifted from 9.62° of MAX to 6.02° of MXene, confirming the presence of a typical layer structure in the MXene nanosheets (Figure S1a). Scanning electron microscope (SEM) images showed that MXene nanosheets have a lightly wrinkled morphology (Figure S1b), and transmission electron microscope (TEM) images displayed a lateral size of hundreds of nanometers and a thickness of single layer to a few layers (Figure S1c). X-ray photoelectron spectroscopy (XPS) of MXene nanosheets demonstrated that they have some terminal groups on their surface, e.g., hydroxyl (−OH) and oxygen (−O) (Figure S1d), which can interact with metal ions via coordination or polydopamine (PD) via hydrogen bonds.[40] In this study, Zn^{2+} was initially chosen as a model metal ion to fabricate a PD-metal ion hybrid (PDZn) percolating nanoscale network in a facile coordination-driven modular assembly method. Percolating nanoscale networks of PDZn can be formed by both the coordination of Zn^{2+} with DA and the oxidative self-polymerization of DA. As shown in the SEM (Figure 1a), there are percolating nanoscale networks in PDZn. PDZn and MXene can be assembled to form porous PDZn@MXene frameworks (Figure 1b, Figure S2).

Regulating the microscale structure of PDZn is a vital factor in the preparation of porous PDZn@MXene as a high-performance gas-sensing material. Thus, evaluating and quantifying complex architectures (e.g., PDZn) with aperiodic stochastic can efficiently guide the synthesis and regulation of the gas-sensing material. Graph theory (GT), a network theory, is a useful tool for quantitatively characterizing and comparing complex architectures.[41,42] By using a Python package of *Structural*GT,[41] we performed GT analysis to convert SEM images of PDZn into a G (n, e) model, consisting of points (nodes, n) connected by lines (edges, e), toward comprehensively describing and comparing the percolating nanoscale networks. As shown in Figure 1c and Figure S3, there are clearly and visually porous structures in PDZn prepared in a 3 h reaction (i.e., PDZn-3 h) via GT analysis. In addition, the degree value of 1 was observed from the degree heatmap due to the occurrence of "structural holes" (Figure S3b), and uniform distribution with value of 1 shows that the "structural holes" have good uniform distribution (Figure S3c). With the reaction time changed from 0.5 to 24 h, PDZn nanoparticles that self-assembled into percolating nanoscale networks increased in size and the "structural holes" uniformity was reduced (Figures S4 and S5). To further quantitatively compare the structures of PDZn prepared at different reaction times, GT parameters were calculated and are listed in Table S1. Comparing these parameters showed that PDZn-3 h had a maximum number of nodes and edges, low average clustering coefficient (Δ), average nodal connectivity (κ), and the highest Wiener index (WI) in the same area. To a certain extent, these results reflected the uniformity, number, and size of pore and van der Waals surface area of PDZn.[43] PDZn-3 h was thus chosen to self-assemble with MXene for the preparation of PDZn@MXene.

SEM images and corresponding energy dispersive X-ray spectroscopy (EDS) mapping of Ti, Zn, and N elements proved the uniform morphology for the large range and uniformly distributed elements in PDZn@MXene (Figure 1d). TEM image of PDZn@MXene displays the loading of the PDZn on MXene nanosheets (Figure S2c), and high-angle annular dark-field-scanning transmission electron microscopy (HAADF-STEM) image and elemental mapping images also further confirm that Zn and N are uniformly distributed in MXene nanosheets (Figure S2d). N_2 adsorption−desorption analysis of PDZn@MXene indicates a typical curve of mesopore structures with a calculated specific surface area (SSA) of 214.4 $m^2 \cdot g^{-1}$ based on the Brunauer−Emmett−Teller method (Figure 1e)[44] and PDZn@MXene had a micro pore at 1.5 nm and a wide pore size distribution from 27 to 108 nm according to the density functional theory (DFT) method (Figure S6). The above results suggest that PDZn@MXene has a three-level hierarchical porous (micro-meso-microporous) structure with a high surface area.

As comparisons, a series of control materials, including PDZnMXene, PD@Zn@MXene, PD@MXene, PD@Zn, and Zn@MXene, were prepared by varying the order of reactant addition (Zn^{2+}, DA, and MXene) and reaction conditions (Figure S7). From the morphological characterization (Figures S8−S11), only PD@Zn@MXene had porous structures due to the existence of percolating nanoscale networks in PD@Zn like PDZn (Figure 1 i-I, Figure S12). These results of elemental mapping images confirm that Zn^{2+} can effectively promote the loading of PD on the surface of MXene nanosheets (Figures S2d and S8−S10). Notably, PDZn@MXene displayed the largest SSA and pore volume compared with MXene and other modified MXene (Figures S13 and S14). X-ray photoelectron spectroscopy (XPS) was used to characterize the surface chemical compositions of pure MXene and the previously mentioned modified MXene (Figure 1f,g, Figures S1d and S15). The C 1s spectrum of PDZn@MXene appeared as C−N peak (285.53 eV), C═O peak (288.44 eV), and $\pi-\pi^*$ peak (291.51 eV), confirming the presence of PD (Figure 1f, Figure S15).[40,45] The C−Ti peak shifted from 282.3 eV of MXene to 281.42 eV for PDZn@MXene, which could be due to the coordination between Zn^{2+} and MXene.[40] PDZn@MXene had peaks of Zn $2p_{1/2}$ (1044.62 eV) and Zn $2p_{3/2}$ (1021.52 eV), confirming the modification of Zn^{2+} (Figure 1g). The atomic content and the ratio of N/Ti and Zn/Ti of pure MXene and modified MXene confirmed that Zn^{2+}-bridge interaction can improve the loading of Zn^{2+} and PD on the surface of MXene nanosheets (Figure S16). The change of ζ potential from −31.9 mV of pure MXene to −9.1 mV of PDZn@MXene indicates the electrostatic attraction involved in Zn^{2+}-bridged interaction (Figure S17). XRD patterns in Figure S18 showed that the 002 peak of PDZnMXene at 4.86° was lower than PD@MXene and disappeared in PDZn@MXene and PD@Zn@MXene, proving the synergetic effect of PD and Zn^{2+} effectively prevents the self-sticking of MXene nanosheets.[44] Meanwhile, the 110 peaks were prominent in PDZnMXene, PD@Zn@MXene, and PDZn@MXene, showing the increase of order in nonbasal directions for MXene nanosheets.[39] To generalize the porous MFs via the coordination-driven modular assembly strategy, a group of chemically modified porous MFs (MFs-1, MFs-2, MFs-3, and MFs-4) were prepared by changing the metal ions, doping

https://doi.org/10.1021/acsnano.2c08266
ACS Nano 2022, 16, 17376−17388

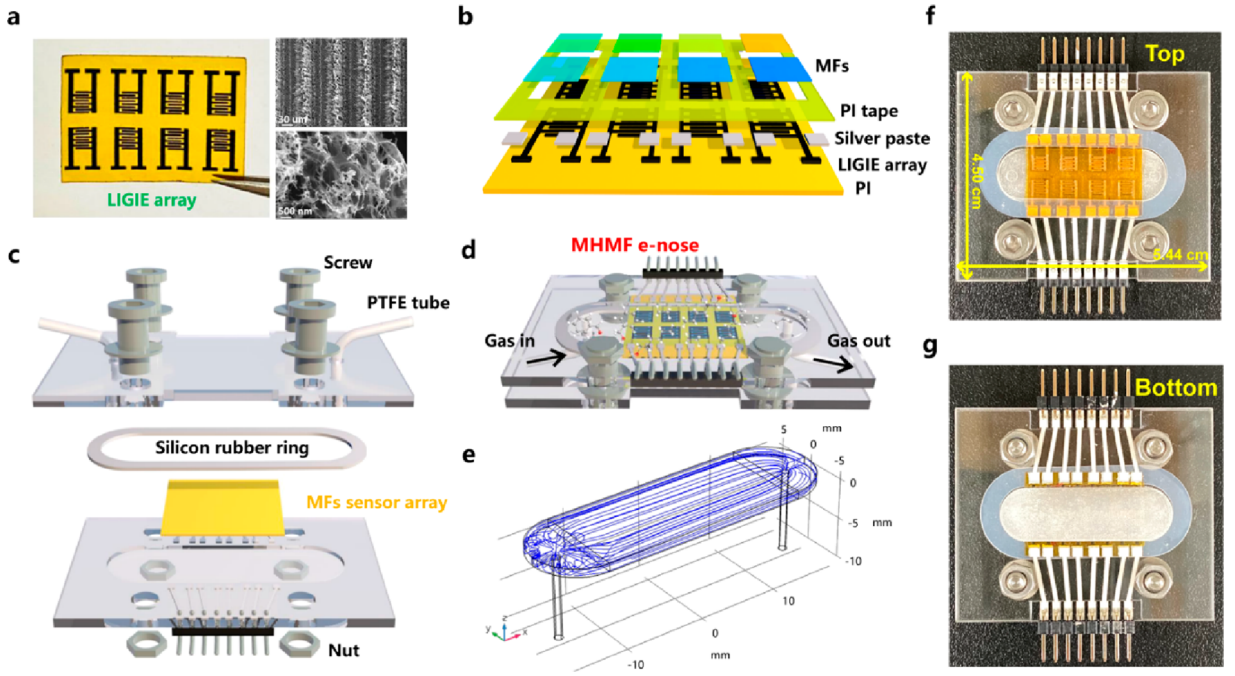

Figure 2. Integrated modular assembly of a MHMF e-nose. (a) Images of the LIGIE array and its SEM characterization. (b) Configuration of a MFs-involved sensor array. (c) Configuration of a laser-engraved microchamber for hosting the MF-involved sensor array. (d) Schematic illustration of the MHMF e-nose. (e) COMSOL simulation of the gas flow in the MHMF e-nose. Photographs of the top (f) and bottom (g) of the MHMF e-nose.

chemical ligands, or regulating reaction sequences to construct different modules (modules-1, modules-2, modules-3, and modules-4) (Figure 1h, Figure S19). Owing to differentiated interaction between metal ions and DA,[46] a series of metal ion-PD hybrids (PDMn, PDCo, PDNi, PDCu, PDCo, and PDFe) as modules-2 can be readily tailored with various structures, which can be assembled with MXene to form distinct metal ion-doped porous MFs (MFs-2, i.e., PDM@MXene, where M represents Mn, Co, Ni, Cu, Fe, and Ca, respectively) (Figure 1j, Figures S19a and S20). Moreover, PD easily reacted with common functional groups (e.g., amine, thiol),[7] and there was also a coordination competition between PD and functional molecules (e.g., 2-methylimidazole).[47] In this situation, some available types of chemical ligands were further applied to tune the properties of modules for assembly (Figure S19b,c), constructing a wealth of ligand-engineered porous MFs (MFs-3 and MFs-4, i.e., PDZnOA$_x$@MXene and PDZn@L@MXene, in which OA$_x$ and L represent different chemical ligands listed in Figure S21). As shown in Figure 1k,l and Figure S22, there were diversified structures in these chemically modified porous MFs. At the same time, the change of reaction sequences of DA, metal ions, and ligands affected the course of coordination-driven assembly for regulating the modules. Using sequence-regulated strategy can further enrich the modules and construct fine-tuned MFs (Figure 1k and Figure S22). Therefore, from the above metal ion-doped, ligand-engineered, and sequence-regulated strategies, a series of differentiated MFs were readily created to provide a rich material basis for constructing a library with desirable and tunable gas-sensing performance.

Integrated Modular Assembly of a MHMF E-Nose. A reliable characterization platform is necessary to evaluate the gas-sensing properties of the as-prepared MFs. We designed and fabricated a compact chamber-sensor-on-a-chip with laser processing technique (Figure 2, Table S2). A 2 × 4 array of LIGIE was directly written on polyimide (PI) film using a CO_2 laser platform, where each electrode has 4 pairs of interdigital fingers with a 200 μm width and 200 μm space (Figure 2a, Figure S23). The laser-writing procedures were carefully optimized by controlling the power of the CO_2 laser and its writing speed. Raman spectrum and SEM were used to evaluate the as-prepared LIGIE (Figures S24 and S25), and optimized parameters of power at 3.5 W and speed at 150 mm/s were obtained for the batch fabrication of LIGIE. After the coating of silver paste and PI tape as a positioning template, the above LIGIE array was set to load 8 types of MFs via a convenient drop-casting operation for the construction of a MFs sensor array (Figure 2b, Figure S26). To host the MFs sensor array, a streamlined gas microchamber was also fabricated by using a CO_2 laser to cut or engrave a poly(methyl methacrylate) (PMMA) plate with holes and groove (Figure 2c, Figure S27). The streamlined groove combined an O-ring rubber with excellent air tightness for the streamlined gas microchamber (Movie S1). As shown in Figure 2c,d, a MHMF e-nose was then assembled with the streamlined gas microchamber, the MFs sensor array, and other accessories. The design of streamlined gas chambers was superior to that of other geometries (such as square-shaped flow chambers)[48] in that the COMSOL simulation confirmed a homogeneous gas distribution in the MHMF e-nose (Figure 2e, Figure S28). There are many advantages regarding our MHMF e-nose. First, it is a chamber-sensor-on-a-chip, highly integrated and compact, with a size of 5.44 cm (L) × 4.50 cm (W) × 0.42 cm (H) (Figure 2f,g). Second, it uses metal clamps and PTFE ferrules to avoid the utilization of glue (Figure S29) and uses an O-ring rubber to ensure the direct contact between LIGIE and the silver stripes on the PMMA plate without sliver pastes. Moreover, our MHMF e-nose can be fabricated with different substrates [e.g., polytetrafluoroethylene (PTFE)] or by using a computerized

https://doi.org/10.1021/acsnano.2c08266
ACS Nano 2022, 16, 17376−17388

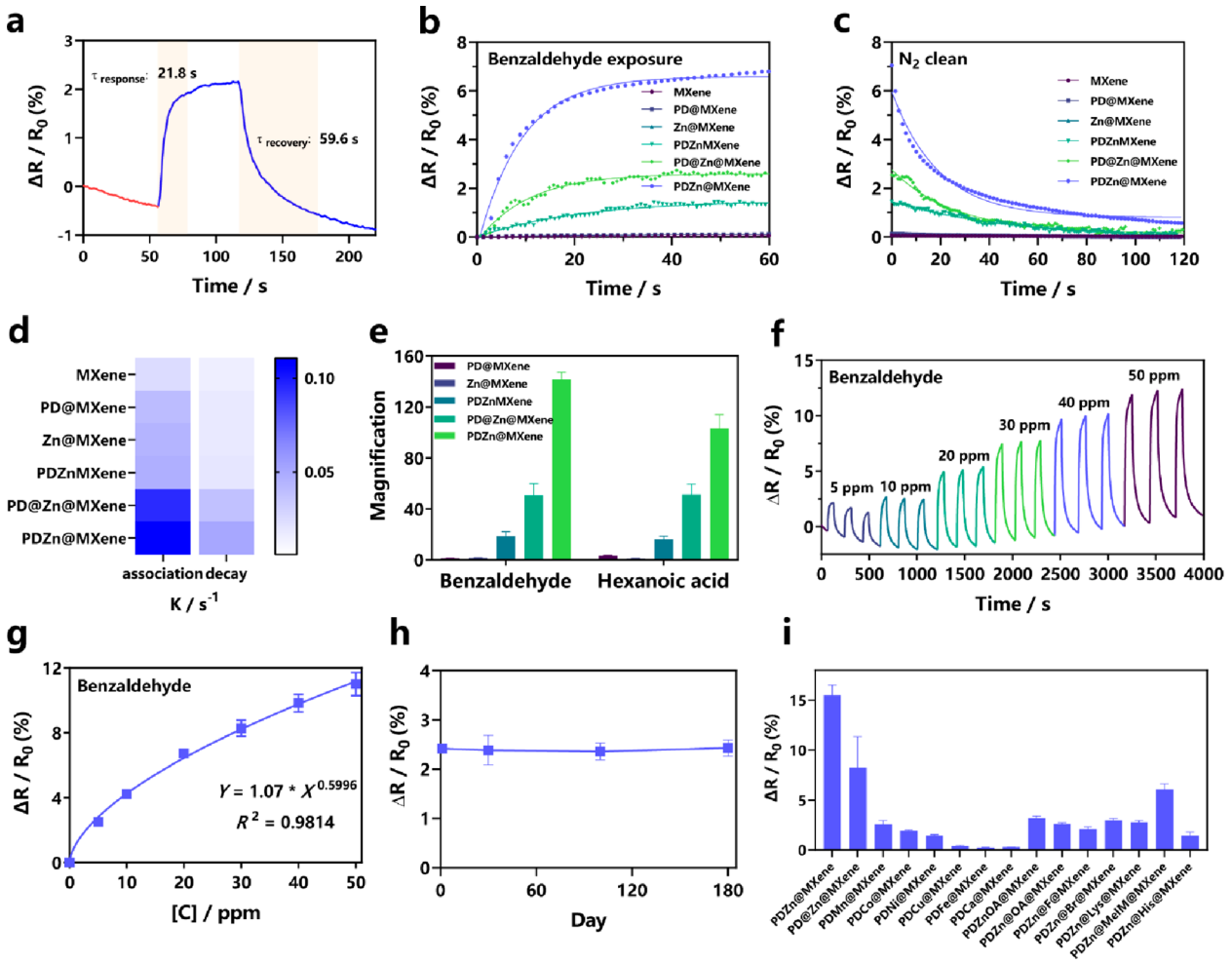

Figure 3. Chemiresistive responses of MXene and modified MXene sensors toward VOCs at room temperature. (a) Response-−recovery time curve for the PDZn@MXene sensor toward 5 ppm benzaldehyde. Kinetic analysis of the chemiresistive responses of the MXene sensor and modified MXene sensors to (b) benzaldehyde exposure (association) and (c) N_2 clean (decay), respectively. (d) Color maps represent the rate constants (K) of MXene sensor and modified MXene sensors to 25 ppm benzaldehyde. (e) Response performances regarding modified MXene sensors toward 25 ppm benzaldehyde and 25 ppm hexanoic acid by compared to that of the MXene sensor. (f) Dynamic response curves of the PDZn@MXene sensor toward benzaldehyde of 5−50 ppm. (g) Relationship of response vs benzaldehyde concentration of the PDZn@MXene sensor. (h) Long-term stability of response over a period of 180 days toward 50 ppm hexanal. PDZn@MXene sensor was stored in a vacuum dryer when it was not used. (i) Chemiresistive response of metal-ion doped, ligand-engineered, and sequences-regulated MFs sensors toward 25 ppm hexanoic acid.

numerical control (CNC) processing method (Figure S30). Thanks to its low-cost, miniaturization, plug-and-play, and replaceability (Figure 2f,g, Table S3), this MHMF e-nose would be used to develop the POCT platform for clinical VOC assays.

VOC-Sensing Performances of the MF Sensors. Using the designed chamber-sensor-on-a-chip, we examined the chemiresistive response of the prepared MXene and modified MXene sensors to VOCs at room temperature (Figure 3). As shown in Figure 3a, the VOC response was defined as the relative change [$\Delta R/R_0(\%)$, $\Delta R = R_{end} - R_0$] in the electrical resistance of MXene and MXene-involved sensors upon the VOC injection (R_{end}) compared to the baseline resistance (R_0) by a homemade gas system (Figure S31). Prior to the injection of VOCs, a typical PDZn@MXene sensor was exposed to pure N_2 gas to stabilize the baseline resistance. Upon exposure to 5 ppm benzaldehyde, the PDZn@MXene sensor achieved a fast response time of 21.8 s and a recovery time of 59.6 s at room temperature (Figure 3a). An ohmic contact was observed between the PDZn@MXene sensor and LIGIE, excluding Schottky barrier modulation (Figure S32). Compared to the MXene-based gas sensors (Table S4), the response and recovery process are greatly accelerated in the PDZn@MXene sensor. In addition, the PDZn@MXene sensor and other control sensors (MXene, PD@MXene, Zn@MXene, PDZnMXene, and PD@Zn@MXene) were, respectively, challenged with 25 ppm benzaldehyde and 25 ppm hexanoic acid in a sequential absorption/desorption process (Figure 3b−e). The chemiresistive responses (CRs) of these sensors to the two VOCs (Figure S33a) were then calculated, and their magnification compared based on MXene sensor (CR_0) [i.e., magnification = $(CR/CR_0 - 1)$]. As depicted in Figure 3e, the PDZn@MXene sensor showed the highest magnification (>100) compared to those of other control sensors. One-phase association/decay, as kinetic models, was used to compare the sensing performance of the above-mentioned sensors (Figure S34). The rate constant (K) of the absorption/desorption process and theoretical achievable responsivity ("Span") of adsorption process were also highest for the PDZn@MXene sensor (Figure 3d, Figure

https://doi.org/10.1021/acsnano.2c08266
ACS Nano 2022, 16, 17376−17388

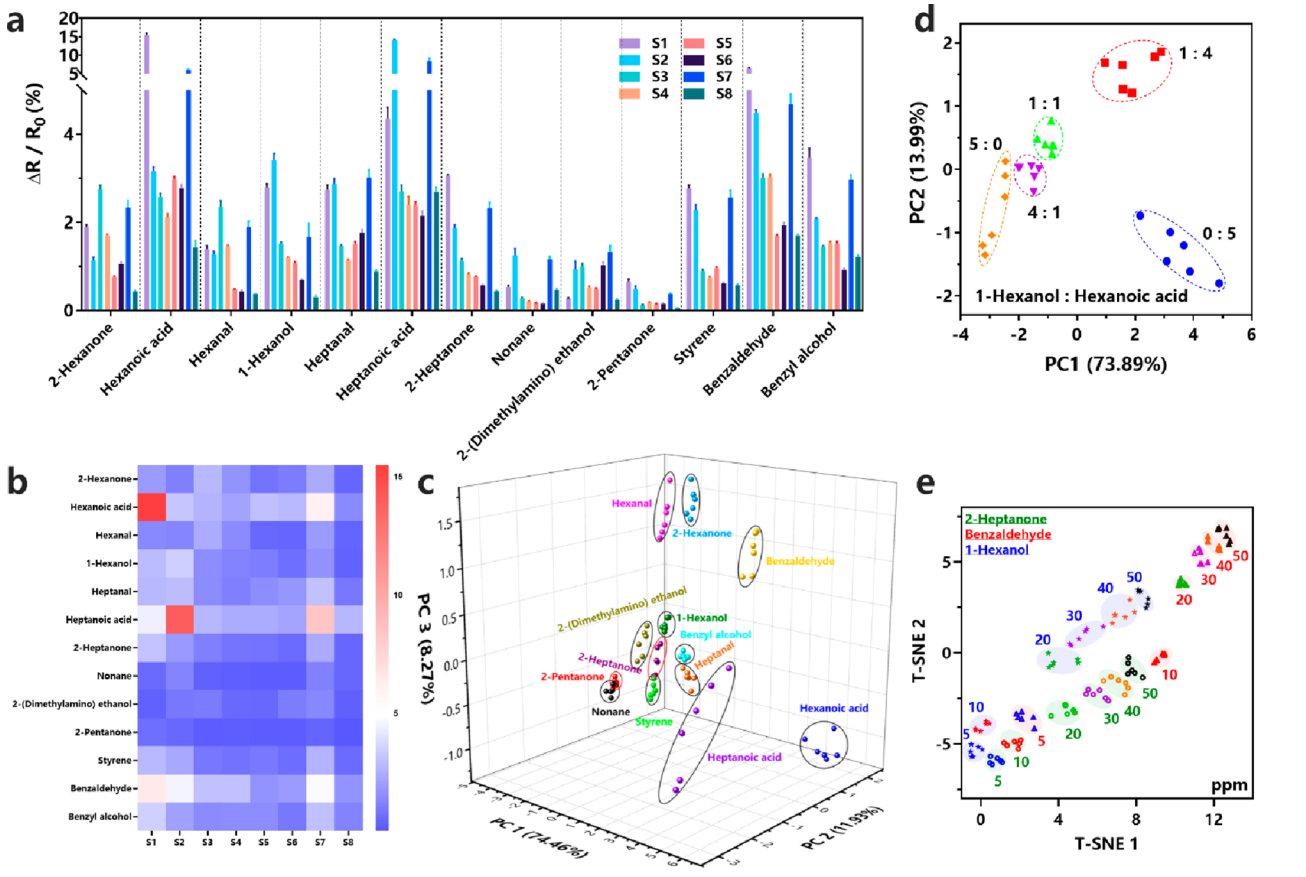

Figure 4. VOC-sensing performances of MHMF e-nose at room temperature. (a) Response performance of the MHMF e-nose toward 13 VOCs at 25 ppm. Error bars represent the mean ± SD. (b) Heatmap of the MHMF e-nose to 13 VOCs at 25 ppm. (c) The corresponding 3D PCA plots toward 13 VOCs at 25 ppm. (d) The 2D PCA plots of the mixture (1-hexanol and hexanoic acid) at different concentration ratios, where the concentration of the mixture is total 50 ppm. (e) 2D T-SNE plots of a varied concentration of 1-hexanol, benzaldehyde, and 2-heptanone from 5 to 50 ppm.

S33b). The above results confirmed that PDZn@MXene has excellent gas-sensing performances when compared to other control sensors. This can be attributed to the following reasons: (1) hierarchical porous structure with high SSA and pore volume help to expand the active surface and accelerate gas diffusion; (2) the synergistic effect of metal ions and PD, a polymer with plentiful aromatic structures and oxygen-contained groups (e.g., −OH), provides multiple interactions (e.g., coordination bond, $\pi-\pi$ conjugate, etc.) with VOCs.

A series of PDZn@MXene sensors made from various reaction conditions were selected as gas-sensing materials to further evaluate the chemiresistive responses when challenged with 25 ppm hexanoic acid (Figures S35 and S36; Table S5). After optimization, the PDZn@MXene-3 h sensor possessed the best chemiresistive response when compared to other PDZn@MXene-0.5 h/6 h/12 h/24 h sensors (Figure S36). These results may be related to the pore size and distribution of PDZn. Therefore, GT analysis is beneficial in building relationships between the materials' structure and gas-sensing property and can guide the synthesis and regulation of gas-sensing materials. All references below to PDZn@MXene stand for PDZn@MXene-3 h unless otherwise specified. Moreover, the PDZn@MXene sensor had a stable chemiresistive response as low as 500 ppb benzaldehyde (Figure S37), with promise for use in ultrasensitive VOC sensing. The dynamic sensing performances of the PDZn@MXene sensor toward 3 VOCs (benzaldehyde, 2-heptanone, and 1-hexanol) were also, respectively, investigated (Figure 3f,g, Figure S38). The output responses were gradually enhanced as the concentrations of VOCs had a higher value and were well-fitted with the power law equation. The universal positive response of the PDZn@MXene sensor is due to the metallic conductivity of MXene, where the VOCs adsorption reduces the number of carriers, leading to the increase of channel resistance. In addition, the PDZn@MXene sensor has great long-term stability over a period of 180 days and shows excellent dynamic repeatability under a 30-cycle response toward 50 ppm hexanal (Figure 3h, Figure S39), which are good in practical applications. A series of MFs, resulting from metal ion-doped, sequence-regulated, and ligand-engineered modifications with optimized ligand dosage, were tested for their chemiresistive responses (Figure 3i, Figure S40). As shown in Figure 3i, there are differential chemiresistive responses for these MFs toward 25 ppm hexanoic acid. These MFs can provide more opportunities for selecting VOC-sensing materials to construct a high-performance e-nose. Microchambers made of PMMA or PTFE with the processing technology of laser or CNC showed excellent gas-sensing performance upon exposure with 50 ppm hexanal over 10 cycles (Figure S41). Figure S41d shows that direct contact between LIGIE and the conductive area of microchamber could substitute for a silver paste adhered connection. Therefore, our designed chamber-sensor-on-a-chip could provide wide prospects for practical gas-sensing applications.

https://doi.org/10.1021/acsnano.2c08266
ACS Nano 2022, 16, 17376−17388

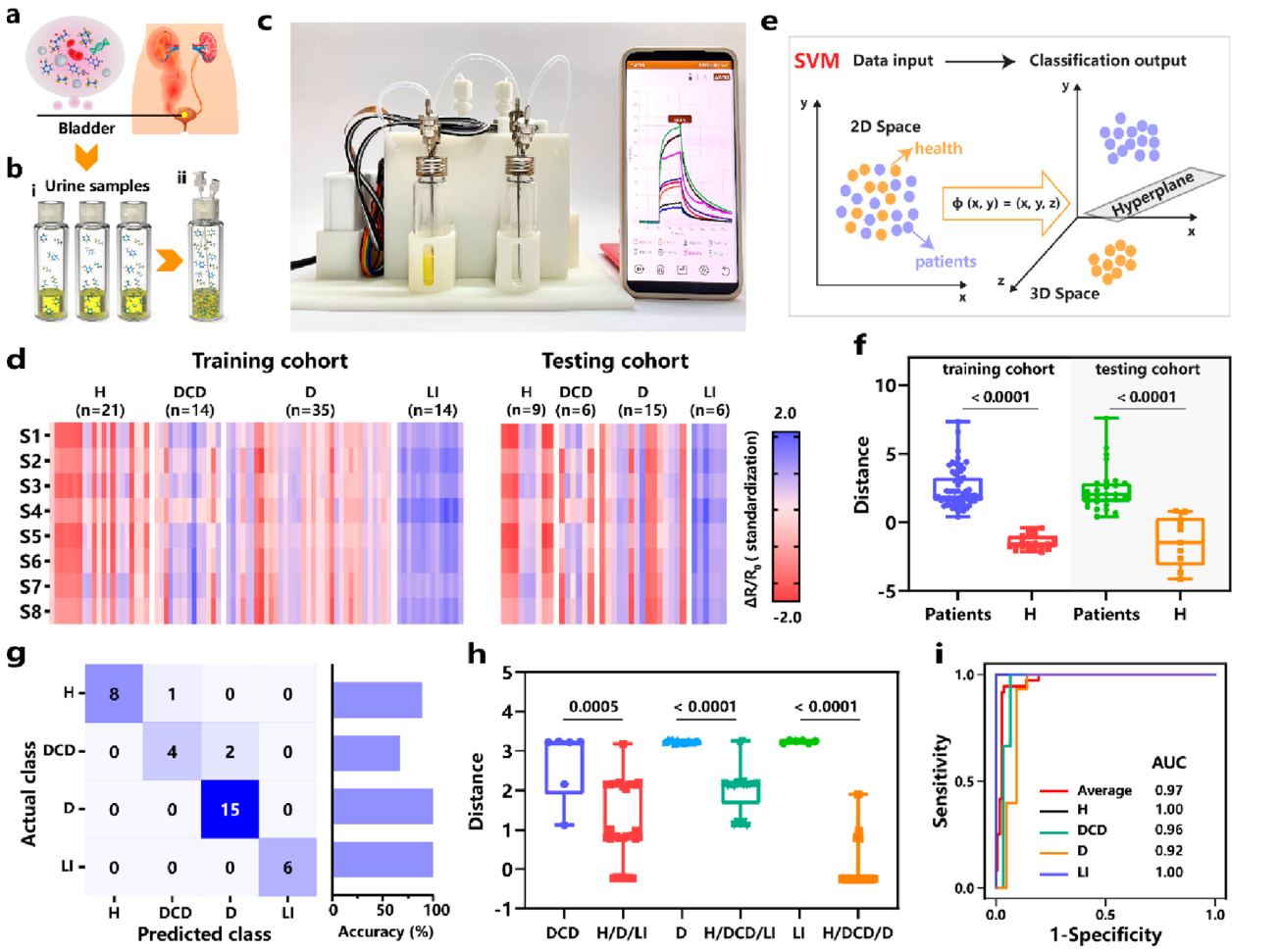

Figure 5. A portable POCT platform for clinical noninvasive disease diagnosis via urinary VOCs assisted with ML algorithm. (a) Schematic illustration of a urinary sample collected from naturally voided urine. (b) Schematic illustration of urinary samples in a 20 mL reagent bottle with a cap containing a PFTE gasket (i) and the reagent bottle inserting 2 stainless steel needles of different lengths for urinary VOCs generation as a bubble bottle (ii). (c) The configured portable POCT platform with a smartphone. (d) Heatmap of $\Delta R/R_0$ (standardization) of MHMF e-nose for the training cohort involving H ($n = 21$), DCD ($n = 14$), D ($n = 35$), and LI ($n = 14$) and the testing cohort involving H ($n = 9$), DCD ($n = 6$), D ($n = 15$), and LF ($n = 6$). (e) Schematic diagram of SVM algorithm for the classification of health and patients. The low-dimensional space was transformed into a high-dimensional space through the inner product function, and the optimal classification was obtained in the space. (f) Box plots of distance values resulting from SVM analysis for comparing between patients and H in the training cohort and testing cohort. (g) Confusion matrix of H, DCD, D, and LI from the classification results by SVM algorithm. (h) Box plots of distance values resulting from SVM analysis for comparing H, DCD, D, and LI in the testing cohort. (i) ROC curves for classifying H and DCD, D, and LI by SVM algorithm. Statistical differences were determined by the two-sided, nonparametric Mann−Whitney test. *P* values are indicted in the charts.

VOC-Sensing Performances of the MHMF E-Nose. Urinary samples are rich in chemical markers, including metabolites, proteins, and different VOCs.[49,50] Detecting urinary VOCs has great potential to diagnose diseases with a range of VOCs markers (acids, alcohols, ketones, aldehydes, amines, N-heterocycles, O-heterocycles, sulfur compounds, and hydrocarbons) in urine.[51−57] One single sensor has extreme difficulty in recognizing multiple VOCs, but an e-nose can detect multiple VOCs via cross-reactivity of the sensor array. Therefore, a sensor array (i.e., e-nose) with highly discriminative recognition is crucial for real applications. With this in mind, we designed a MF-involved 8-channel sensor array in the MHMF e-nose and integrated 8 MFs-based sensors (S1−S8) as sensor arrays (Table S6). To test the discriminative performance of the MHMF e-nose, 13 types of disease-related VOCs were selected (Figure S42). Figure 4a,b presents the response and heatmap of MHMF e-nose toward 13 VOCs at 25 ppm. The results demonstrate that the MHMF e-nose can produce differentiated response patterns. Principal component analysis (PCA)[58] and t-distributed stochastic neighbor embedding (T-SNE)[59] were employed to differentiate and visualize the response patterns of the MHMF e-nose toward VOCs. Extracted features of relative change (F_1−F_8) were used to perform PCA and T-SNE. We employed three-dimensional (3D) PCA plots to successfully discriminate 13 VOCs (Figure 4c). Noticeably, there are some overlaps by using two-dimensional (2D) PCA plots for discriminating 13 VOCs (Figure S43a). Compared with PCA, T-SNE as a nonlinear dimensionality reduction, often has a better effect on feature dimension reduction and visualization. 2D T-SNE plots can replace 3D PCA plots to identify 13 VOCs (Figure S43) and confirm that T-SNE has a more robust pattern recognition for the application of the MHMF e-nose.

To further explore the performance of the MHMF e-nose, mixed VOCs at different concentration ratios (1-hexanol:hexanoic acid, 5:0, 4:1, 1:1, 1:4, and 0:5, total 50 ppm) and 3 VOCs at a series of concentration gradients (1-hexanol, 2-heptanone,

https://doi.org/10.1021/acsnano.2c08266
ACS Nano 2022, 16, 17376−17388

and benzaldehyde from 5 to 50 ppm) were tested. As shown in Figure S44 and Figure 4d, the MHMF e-nose performed a differentiated response pattern with a clear separation of clusters toward mixed VOCs. Moreover, the MHMF e-nose also had a response pattern to 3 VOCs from 5 to 50 ppm (Figure S45a,b). PCA and T-SNE both can discriminate 2 VOCs (1-heptanone and 1-hexanol) at different concentration gradients (Figure S45c,d). Notably, PCA failed to recognize 3 VOCs at concentration gradients; however, T-SNE successfully recognized them (Figure 4e, Figure S45e). The results demonstrate that T-SNE often has a stronger function in the field of e-noses and the MHMF e-nose performs highly discriminative recognition toward VOCs-related analysis.

Modular Assembly of a Portable POCT Platform for Clinical Noninvasive Disease Diagnosis. Benefiting from the MHMF e-nose, a portable POCT platform was developed for clinical noninvasive disease diagnosis via urinary VOCs. As shown in Figure 5a,b, 120 cases of urinary samples, including health (H, $n = 30$), patients with DCD ($n = 20$), D ($n = 50$) and LI ($n = 20$), were collected and placed in homemade bubble bottles, respectively. The POCT platform composed of a gas path-controlled module, MHMF e-nose module, and a signal reading module designed by SolidWorks software (Figures S46−S48). It is worth noting that the modular design allows the easy assembly for these modules and replacement for maintenance and portability (Movie S2). Combined with a smartphone, the POCT platform can successfully achieve a signal reading in a wireless and real-time format (Figure 5c). The POCT platform was then used to "smell" the VOCs of urinary samples ($n = 120$). 2D T-SNE shows a small improvement in H and disease groups recognition than 2D PCA, but only through the simple and direct visualization on a 2D plane map by using PCA or T-SNE and is not ideal for accurate diagnosis (Figure S49).

A ML algorithm was constructed in the diagnostic model due to its great performance in handling complex clinical data.[60−62] The obtained data were shuffled randomly. The 70% data were used as a training data set and the other 30% as a testing data set. Figure 5d shows the differentiation of urinary VOC-related fingerprints among the H group and disease groups (patients with D, DCD, and LI). Considering that different algorithms often cause differences among predicted results, 4 ML algorithms, including support vector machine (SVM), *k*-nearest neighbor (KNN), random forest (RF), and artificial neural network (ANN), were selected to discriminate the health subjects and patients. Figure S50 and Table S7 show that the SVM model (Figure 5e) has a better diagnostic performance than the other models between H group ($n = 30$) and patients ($n = 90$) (accuracy: 94.4%, specificity: 77.8%, sensitivity: 100%). According to the SVM model, the receiver operating characteristic (ROC) analysis was used to further evaluate the diagnostic performance. The value of area under the ROC curve (AUC) was calculated as 0.98, and box plots of distance values resulting from SVM analysis confirm that the difference between the patients and H group ($P < 0.05$) (Figure S51 and Figure 5f). These results show that the SVM model can perform a good classification. To further explore the capacity of the POCT platform for disease diagnosis, H group and 3 types of disease groups (patients with DCD: $n = 20$, D: $n = 50$, and LI: $n = 20$) were classified with a multiclass classification method. Compared to other models, the SVM model still presents the best performance (average accuracy: 91.7%, average specificity: 96.8%, and average sensitivity: 88.9%) (Figure 5g, Figure S52 and Table S8). In addition, box plots of distance values further confirm that H, DCD, D, and LI can be greatly discriminated based on SVM algorithm ($P < 0.05$) (Figure 5h and Figure S53), and the AUC of each group and overall have a high value (Figure 5i). All the above-mentioned results show that the high-performance classification for H group and 3 types of disease groups can be also achieved by the SVM algorithm. In comparison with other studies of disease diagnosis based on body fluids or breath (Table S9), our POCT platform has excellent competitive capacity to realize real-time, noninvasive, and accurate diagnosis of multiple diseases assisted by the ML algorithm.

CONCLUSION

To sum up, a versatile coordination-driven modular assembly strategy was created to produce a library of MXene frameworks (MFs) with adjustable properties, providing an abundant material basis for the development of high-performance e-noses. The marriage of a MF-involved sensor array and a well-designed laser-engraved microchamber fuels the integrated modular assembly of a cost-effective, ingenious, and highly discriminative chamber-sensor-on-a-chip (i.e., MHMF e-nose) that simultaneously senses and distinguishes complex VOCs. More importantly, a portable POCT platform integrated with the MHMF e-nose was modularly configured and used for real-time and wireless monitoring of urinary VOCs to achieve noninvasive, rapid, and accurate diagnoses of multiple diseases assisted with the ML algorithm. This work offers a promising prospect for the development of robust and noninvasive diagnostic strategies in a clinical setting.

METHODS

Preparation of MXene Nanosheets. MXene was prepared by a freeze−thaw-assisted method. Briefly, 1.0 g of LiF was dissolved in 20 mL of 9 M HCl and stirred for 5 min. Then 1.0 g of Ti_3AlC_2 (MAX) was slowly added to the above solution (~20 min). Next, the mixture was placed in an oil bath and stirred at 35 °C for 48 h. After etching, the mixture was washed with H_2O by centrifugation until pH 7.0 to obtain multilayer MXene (m-MXene). 70 mL of H_2O was added to m-MXene and argon gas (Ar) was injected for several minutes. Then, the m-MXene was frozen in the refrigerator (−20 °C) and then thawed at room temperature. The freeze−thaw step was repeated for 3 cycles. After that, the dispersion was ultrasonicated for 40 min in ice bath and Ar atmosphere. Finally, the dispersion was centrifuged at 3500 rpm for 30 min to obtain the supernatant, which is MXene nanosheets. The concentration of MXene nanosheets was determined via UV−vis measurement.

Preparation of MXene Frameworks. A facile coordination-driven modular assembly strategy was presented in our work, in which MXene frameworks (MFs) were prepared by varying the mixing amount of DA·HCl, $Zn(CH_3COO)_2{\cdot}2H_2O$, and MXene and tuning the reaction time of DA and Zn^{2+} after the addition of NaOH. The detailed information regarding procedures, reagent dosages, and reaction time are depicted in Figure S7 and Table S5. Taking the preparation of PDZn@MXene as an example: 12.5 mg of DA·HCl and 0.2 mmol $Zn(CH_3COO)_2{\cdot}2H_2O$ were dissolved into 50 mL of H_2O and stirred at room temperature for 5 min. Then, 500 μL of NaOH (0.5 M) was added into the above solution and stirred for 3 h. Next, 5 mL of MXene (5 mg/mL) was added slowly and stirred for 1 h. After that, the mixture was centrifuged and washed with anhydrous ethanol to obtain the precipitate of PDZn@MXene, which was further dried in a vacuum oven at room temperature until ethanol was almost removed. Finally, the powder was redispersed in 6 mL of anhydrous ethanol via oscillation and sonication to form the resulting solution of PDZn@MXene. In a similar way, a group of control materials were prepared including PDZnMXene, PD@Zn@MXene, PD@MXene, and Zn@MXene. A

https://doi.org/10.1021/acsnano.2c08266
ACS Nano 2022, 16, 17376−17388

series of chemically modified MFs were also prepared by changing the metal ions (Cu^{2+}, Ca^{2+}, Ni^{2+}, Co^{3+}, Mn^{2+}, and Fe^{2+}) or doping chemical ligands (OA, Br, MeIM, Lys, His, and F). Detailed information is presented in Figures S19 and S21.

Structural Analysis of PDZn and PD@Zn via GT. *Structural*GT, an open-source Python software package (Github page: https://github.com/drewvecchio/StructuralGT), was created by Drew A. Vecchio et al. for automated structural analysis. The SEM images of PD@Zn and PDZn with different reaction time were imported to *Structural*GT and then processed by choosing the settings of "OTSU Threshold" and "Apply gaussian blur"; at the same time, removing disconnected segments in the resulting graphs of the images to obtain a more accurate connectivity value. Finally, corresponding settings in the region of "NetworkX Calculation Settings" were selected in order to obtain each needed GT parameter and image. All SEM images were not altered by other image processing software.

Fabrication of LIGIE Array, MFs Sensor Array, and Microchamber. A 2 × 4 array of LIGIE was fabricated on PI film (1 mm) using a CO_2 laser platform, in which each electrode has 4 pairs of interdigital electrodes with a 200 μm width and 200 μm space (Figure S23). A VOCs sensor array was fabricated via drop-casting of MFs including PDZn@MXene, PDZnOA@MXene, and PDZn@L@MXene (L: OA, Br, MelM, Lys, His, and F) onto the LGIE array (Figure S26). A VOCs sensing microchamber was fabricated via laser or CNC process of PMMA or PTFE, blade-casting of silver paste, equipping with pin headers, and assembling with MFs sensor array (MHMF e-nose) (Figure S27). Table S2 summarizes detailed parameters for the fabrication of laser-induced graphene interdigital electrode array (LGIE array) and our proposed MHMF e-nose.

Design and Fabrication of the Portable POCT Platform. The portable device, including gas path control module, sensor module, and signal reading module (Figures S46 and S47), was designed by SolidWorks software. Module attachments prototyped by a 3D printer (UnionTech 600). Micropump (T5-1IC-03-1EEP, Parker Hannifin) with three AAA batteries and three-way miniature solenoid valves with 24 V power switch were installed at the gas-path control module for pulling urinary VOCs from the bubble bottle and buffer bottle onto the MHMF e-nose and cleaning VOCs. A portable eight-channel resistance tester (LZ-01ARC, Hangzhou LinkZill Technology Co., Ltd.) combined with an Android smartphone was used to construct signal reading module by wireless monitoring.

ASSOCIATED CONTENT

Supporting Information

The Supporting Information is available free of charge at https://pubs.acs.org/doi/10.1021/acsnano.2c08266.

Materials and instrumentations used in this work; supplemental experimental methods; VOC gas-sensing test; clinical urinary sample collection and testing; computational fluid dynamics simulation; XRD patterns of MAX, pure MXene and modified MXene; XPS spectra, N_2 adsorption−desorption isotherms, SSA, pore volume and Zeta potential of pure MXene and modified MXene; pore size distribution of PDZn@MXene; SEM images of pure MXene, modified MXene, PDM, PDZn, PD@Zn, MFs, and PDZn reacted with different types of chemical ligands; TEM and HAADF-STEM images of pure and modified MXene; structural analysis of PDZn and PD@Zn via GT; large-scale direct writing LIGIE array; photograph of LIG mapping; optimized parameters and Raman spectrum of LIG; the fabrication of LIGIE array, MFs sensor array, and microchamber; photographs of homemade microchambers; homemade gas system for detection of VOCs at given concentrations; linear I−V curve for PDZn@MXene sensor fabricated on LIGIE; response performances regarding MXene sensor and modified MXene sensors; kinetic models; chemiresistive responses of a series of PDZn@MXene sensors made from different mass ratio (MXene: DA: Zn^{2+}) and different reaction time of DA and Zn^{2+}; dynamic response curves and consecutive cyclic dynamic response of PDZn@MXene sensor; chemresistive responses of PDZnOA$_x$@MXene; name and chemical formulas of the selected VOCs; VOC-sensing performances of MHMF e-nose; the configuration and size of portable POCT platform; 2D PCA and 2D T-SNE from H and patients (DCD, D, LI); confusion matrices and ROC curves of H and patients from the classification results by KNN, RF, ANN, and SVM; Confusion matrixes of H, DCD, D, and LI from the classification results by KNN, RF, and ANN; box plots of distance values resulting from SVM analysis for comparing H, DCD, D, and LI in the training cohort; tables summarizing selected GT parameters and parameters for the fabrication of LGIE array and MHMF e-nose; summary of microchamber with different processing methods and materials; response/recovery time of MXene-based sensors from other studies and this work; different formulas and parameters for the preparation of various PDZn@MXene; information on selected sensors to construct MHMF e-nose; tables summarizing comparison of evaluation parameters with different ML algorithms; performances comparison between our POCT platform and previously reported methods for disease diagnosis (PDF)

Movie S1: Air tightness test for MHMF e-nose (MP4)

Movie S2: The process of modular assembly for the portable POCT (MP4)

AUTHOR INFORMATION

Corresponding Authors

Min Zhang − *School of Chemistry and Molecular Engineering, Shanghai Key Laboratory for Urban Ecological Processes and Eco-Restoration, Engineering Research Centre for Nanophotonics and Advanced Instrument (Ministry of Education), East China Normal University, Shanghai 200241, China*; orcid.org/0000-0001-5108-1275; Email: mzhang@chem.ecnu.edu.cn

Hossam Haick − *Department of Chemical Engineering and Russell Berrie Nanotechnology Institute, Technion - Israel Institute of Technology, 320003 Haifa, Israel*; orcid.org/0000-0002-2370-4073; Email: hhossam@technion.ac.il

Authors

Xuyin Ding − *School of Chemistry and Molecular Engineering, Shanghai Key Laboratory for Urban Ecological Processes and Eco-Restoration, Engineering Research Centre for Nanophotonics and Advanced Instrument (Ministry of Education), East China Normal University, Shanghai 200241, China*

Yecheng Zhang − *College of Architecture and Art, Hefei University of Technology, Hefei 230601, China*

Yue Zhang − *Bengbu Medical University, Anhui Provincial Hospital, Bengbu 233030, China*

Xufa Ding − *School of Mechanical Engineering, Hefei University of Technology, Hefei 230601, China*

Hanxin Zhang − *School of Chemistry and Molecular Engineering, Shanghai Key Laboratory for Urban Ecological Processes and Eco-Restoration, Engineering Research Centre for Nanophotonics and Advanced Instrument (Ministry of*

https://doi.org/10.1021/acsnano.2c08266
ACS Nano 2022, 16, 17376−17388

Education), East China Normal University, Shanghai 200241, China

Tian Cao − *School of Chemistry and Molecular Engineering, Shanghai Key Laboratory for Urban Ecological Processes and Eco-Restoration, Engineering Research Centre for Nanophotonics and Advanced Instrument (Ministry of Education), East China Normal University, Shanghai 200241, China*

Zhi-bei Qu − *Department of Medicinal Chemistry, School of Pharmacy, Fudan University, Shanghai 201203, China;* orcid.org/0000-0003-1517-0822

Jing Ren − *School of Chemistry and Molecular Engineering, Shanghai Key Laboratory for Urban Ecological Processes and Eco-Restoration, Engineering Research Centre for Nanophotonics and Advanced Instrument (Ministry of Education), East China Normal University, Shanghai 200241, China*

Lei Li − *Department of Infectious Disease, The First Affiliated Hospital, University of Science and Technology of China, Hefei 230001, China*

Zhijun Guo − *Department of Pharmacy, Sixth People's Hospital South Campus, Shanghai Jiao Tong University, Shanghai 201499, China*

Feng Xu − *Department of Pharmacy, Sixth People's Hospital South Campus, Shanghai Jiao Tong University, Shanghai 201499, China*

Qi-Xian Wang − *College of Chemistry and Molecular Engineering, Peking University, Beijing 100871, China*

Xing Wu − *School of Communication and Electronic Engineering, East China Normal University, Shanghai 200241, China*

Guoyue Shi − *School of Chemistry and Molecular Engineering, Shanghai Key Laboratory for Urban Ecological Processes and Eco-Restoration, Engineering Research Centre for Nanophotonics and Advanced Instrument (Ministry of Education), East China Normal University, Shanghai 200241, China;* orcid.org/0000-0002-5900-2209

Complete contact information is available at: https://pubs.acs.org/10.1021/acsnano.2c08266

Notes

The authors declare no competing financial interest.

ACKNOWLEDGMENTS

This work was supported by the National Natural Science Foundation of China (22274053, 22274051), the funds of Shanghai Science and Technology Committee (19ZR1473300, 19411971700), the director fund of Shanghai Key Lab for Urban Ecological Processes and Eco-Restoration (SHUES2022C03), the fund of Shanghai Key Laboratory of Multidimensional Information Processing (MIP202104), the fund of Shanghai Municipal Science and Technology Major Project ("Beyond Limits manufacture"), and the Fundamental Research Funds for the Central Universities.

REFERENCES

(1) Yang, J.; Wang, R.; Huang, L.; Zhang, M.; Niu, J.; Bao, C.; Shen, N.; Dai, M.; Guo, Q.; Wang, Q.; Wang, Q.; Fu, Q.; Qian, K. Urine Metabolic Fingerprints Encode Subtypes of Kidney Diseases. *Angew. Chem., Int. Ed.* **2020**, *59*, 1703−1710.

(2) Seol, W.; Kim, H.; Son, I. Urinary Biomarkers for Neurodegenerative Diseases. *Exp. Neurobiol.* **2020**, *29*, 325−333.

(3) Da Costa, B. R. B.; De Martinis, B. S. Analysis of urinary VOCs using mass spectrometric methods to diagnose cancer: A review. *Clin. Mass Spectrom.* **2020**, *18*, 27−37.

(4) Tyagi, H.; Daulton, E.; Bannaga, A. S.; Arasaradnam, R. P.; Covington, J. A. Urinary Volatiles and Chemical Characterisation for the Non-Invasive Detection of Prostate and Bladder Cancers. *Biosensors* **2021**, *11*, 437.

(5) Baldini, C.; Billeci, L.; Sansone, F.; Conte, R.; Domenici, C.; Tonacci, A. Electronic Nose as a Novel Method for Diagnosing Cancer: A Systematic Review. *Biosensors* **2020**, *10*, 84.

(6) Peng, G.; Tisch, U.; Adams, O.; Hakim, M.; Shehada, N.; Broza, Y. Y.; Billan, S.; Abdah-Bortnyak, R.; Kuten, A.; Haick, H. Diagnosing lung cancer in exhaled breath using gold nanoparticles. *Nat. Nanotechnol.* **2009**, *4*, 669−673.

(7) Zhang, M.; Sun, J. J.; Khatib, M.; Lin, Z. Y.; Chen, Z. H.; Saliba, W.; Gharra, A.; Horev, D. Y.; Kloper, V.; Milyutin, Y.; Huynh, T. P.; Brandon, S.; Shi, G.; Haick, H. Time-space-resolved origami hierarchical electronics for ultrasensitive detection of physical and chemical stimuli. *Nat. Commun.* **2019**, *10*, 1120.

(8) Zhang, M.; Fan, Y. L.; Lu, Y. F.; Ding, X. Y.; Lin, Z. Y.; Shi, G.; Wu, W. W.; Haick, H. Tailor-Made Engineering of Bioinspired Inks for Writing Barcode-like Multifunctional Sensory Electronics. *ACS Sens* **2019**, *4*, 2588−2592.

(9) Einoch-Amor, R.; Broza, Y. Y.; Haick, H. Detection of Single Cancer Cells in Blood with Artificially Intelligent Nanoarray. *ACS Nano* **2021**, *15*, 7744−7755.

(10) Kang, H.; Cho, S. Y.; Ryu, J.; Choi, J.; Ahn, H.; Joo, H.; Jung, H. T. Multiarray Nanopattern Electronic Nose (E-Nose) by High-Resolution Top-Down Nanolithography. *Adv. Funct. Mater.* **2020**, *30*, 2002486.

(11) Liang, H.; Zhang, H.; Sun, H.; Jin, H.; Zhang, X.; Jin, Q.; Zou, J.; Haick, H.; Jian, K. Light-Regulated Electrochemical Sensor Array for Efficiently Discriminating Hazardous Gases. *ACS Sens* **2017**, *2*, 1467−1473.

(12) Deng, Y.; Sun, J.; Jin, H.; Khatib, M.; Li, X.; Wei, Z.; Wang, F.; Horev, Y. D.; Wu, W.; Haick, H. Chemically Modified Polyaniline for the Detection of Volatile Biomarkers of Minimal Sensitivity to Humidity and Bending. *Adv. Healthcare Mater.* **2018**, *7*, 1800232.

(13) Abbas, A. N.; Liu, B. L.; Chen, L.; Ma, Y.; Cong, S.; Aroonyadet, N.; Kopf, M.; Nilges, T.; Zhou, C. Black Phosphorus Gas Sensors. *ACS Nano* **2015**, *9*, 5618−5624.

(14) Jian, Y.; Hu, W.; Zhao, Z.; Cheng, P.; Haick, H.; Yao, M.; Wu, W. Gas Sensors Based on Chemi-Resistive Hybrid Functional Nanomaterials. *Nano-Micro Lett.* **2020**, *12*, 71.

(15) Li, Z.; Liu, Y.; Hossain, O.; Paul, R.; Yao, S.; Wu, S.; Ristaino, J. B.; Zhu, Y.; Wei, Q. Real-time monitoring of plant stresses via chemiresistive profiling of leaf volatiles by a wearable sensor. *Matter* **2021**, *4*, 2553−2570.

(16) Campbell, M. G.; Liu, S. F.; Swager, T. M.; Dincă, M. Chemiresistive Sensor Arrays from Conductive 2D Metal−Organic Frameworks. *J. Am. Chem. Soc.* **2015**, *137*, 13780−13783.

(17) Wang, R.; Lan, K.; Chen, Z.; Zhang, X.; Hung, C. T.; Zhang, W.; Wang, C.; Wang, S.; Chen, A.; Li, W.; Xu, X.; Zhao, D. Janus Mesoporous Sensor Devices for Simultaneous Multivariable Gases Detection. *Matter* **2019**, *1*, 1274−1284.

(18) Wu, J.; Wei, Y.; Ding, H.; Wu, Z.; Yang, X.; Li, Z.; Huang, W.; Xie, X.; Tao, K.; Wang, X. Green Synthesis of 3D Chemically Functionalized Graphene Hydrogel for High-Performance NH_3 and NO_2 Detection at Room Temperature. *ACS Appl. Mater. Interfaces* **2020**, *12*, 20623−20632.

(19) Chen, H.; Min, X.; Hui, Y.; Qin, W.; Zhang, B.; Yao, Y.; Xing, W.; Zhang, W.; Zhou, N. Colloidal oxide nanoparticle inks for micrometer-resolution additive manufacturing of three-dimensional gas sensors. *Mater. Horiz.* **2022**, *9*, 764−771.

(20) Fu, J. H.; Zhong, Z.; Xie, D.; Guo, Y. J.; Kong, D. X.; Zhao, Z. X.; Zhao, Z. X.; Li, M. SERS-Active MIL-100(Fe) Sensory Array for Ultrasensitive and Multiplex Detection of VOCs. *Angew. Chem., Int. Ed.* **2020**, *59*, 20489−20498.

(21) Broomell, C. C.; Mattoni, M. A.; Zok, F. W.; Waite, J. H. Critical role of zinc in hardening of Nereis jaws. *J. Exp. Biol.* **2006**, *209*, 3219−3225.
(22) Qu, Z.; Feng, W.; Wang, Y.; Romanenko, F.; Kotov, N. A. Diverse Nanoassemblies of Graphene Quantum Dots and Their Mineralogical Counterparts. *Angew. Chem., Int. Ed.* **2020**, *59*, 8542−8551.
(23) Priemel, T.; Palia, G.; Förste, F.; Jehle, F.; Sviben, S.; Mantouvalou, I.; Zaslansky, P.; Bertinetti, L.; Harrington, M. J. Microfluidic-like fabrication of metal ion−cured bioadhesives by mussels. *Science* **2021**, *374*, 206−211.
(24) Guo, J.; Tardy, B. L.; Christofferson, A. J.; Dai, Y.; Richardson, J. J.; Zhu, W.; Hu, M.; Ju, J.; Cui, Y.; Dagastine, R. R.; Yarovsky, I.; Caruso, F. Modular assembly of superstructures from polyphenol-functionalized building blocks. *Nat. Nanotechnol.* **2016**, *11*, 1105−1111.
(25) Ai, Y.; Sun, H.; Gao, Z.; Wang, C.; Guan, L.; Wang, Y.; Wang, Y.; Zhang, H.; Liang, Q. Dual Enzyme Mimics Based on Metal−Ligand Cross-Linking Strategy for Accelerating Ascorbate Oxidation and Enhancing Tumor Therapy. *Adv. Funct. Mater.* **2021**, *31*, 2103581.
(26) Zou, Z.; He, L.; Deng, X.; Wang, H.; Huang, Z.; Xue, Q.; Qing, Z.; Lei, Y.; Yang, R.; Liu, J. Zn^{2+}-Coordination-Driven RNA Assembly with Retained Integrity and Biological Functions. *Angew. Chem., Int. Ed.* **2021**, *60*, 22970−22976.
(27) Huang, Y.; Gao, Q.; Li, C.; Chen, X.; Li, X.; He, Y.; Jin, Q.; Ji, J. Facile Synthesis of Zn^{2+}-Based Hybrid Nanoparticles as a New Paradigm for the Treatment of Internal Bacterial Infections. *Adv. Funct. Mater.* **2022**, *32*, 2109011.
(28) Kim, S. J.; Koh, H. J.; Ren, C. E.; Kwon, O.; Maleski, K.; Cho, S. Y.; Anasori, B.; Kim, C. K.; Choi, Y. K.; Kim, J.; Gogotsi, Y.; Jung, H. T. Metallic Ti3C2Tx MXene Gas Sensors with Ultrahigh Signal-to-Noise Ratio. *ACS Nano* **2018**, *12*, 986−993.
(29) Koh, H. J.; Kim, S. J.; Maleski, K.; Cho, S. Y.; Kim, Y. J.; Ahn, C. W.; Gogotsi, Y.; Jung, H. T. Enhanced Selectivity of MXene Gas Sensors through Metal Ion Intercalation: In Situ X-ray Diffraction Study. *ACS Sens* **2019**, *4*, 1365−1372.
(30) Chen, W. Y.; Jiang, X.; Lai, S. N.; Peroulis, D.; Stanciu, L. Nanohybrids of a MXene and transition metal dichalcogenide for selective detection of volatile organic compounds. *Nat. Commun.* **2020**, *11*, 1302.
(31) Chen, W. Y.; Lai, S. N.; Yen, C. C.; Jiang, X.; Peroulis, D.; Stanciu, L. A. Surface Functionalization of Ti3C2Tx MXene with Highly Reliable Superhydrophobic Protection for Volatile Organic Compounds Sensing. *ACS Nano* **2020**, *14*, 11490−11501.
(32) Li, X.; An, Z.; Lu, Y.; Shan, J.; Xing, H.; Liu, G.; Shi, Z.; He, Y.; Chen, Q.; Han, R. P. S.; Wang, D.; Jiang, J.; Zhang, F.; Liu, Q. Room Temperature VOCs Sensing with Termination-Modified $Ti_3C_2T_x$ MXene for Wearable Exhaled Breath Monitoring. *Adv. Mater. Technol.* **2022**, *7*, 2100872.
(33) Fernandez, E.; Saiz, P. G.; Peřinka, N.; Wuttke, S.; Fernández de Luis, R. Printed Capacitive Sensors Based on Ionic Liquid/Metal-Organic Framework Composites for Volatile Organic Compounds Detection. *Adv. Funct. Mater.* **2021**, *31*, 2010703.
(34) Kim, Y. S.; Ha, S. C.; Yang, H.; Kim, Y. T. Gas sensor measurement system capable of sampling volatile organic compounds (VOCs) in wide concentration range. *Sensor Actuat. B-Chem.* **2007**, *122*, 211−218.
(35) Klank, H.; Kutter, J. P.; Geschke, O. CO_2-laser micromachining and back-end processing for rapid production of PMMA-based microfluidic systems. *Lab Chip* **2002**, *2*, 242−246.
(36) Lin, J.; Peng, Z.; Liu, Y.; Ruiz-Zepeda, F.; Ye, R.; Samuel, E. L.; Yacaman, M. J.; Yakobson, B. I.; Tour, J. M. Laser-induced porous graphene films from commercial polymers. *Nat. Commun.* **2014**, *5*, 5714.
(37) Yang, L.; Yi, N.; Zhu, J.; Cheng, Z.; Yin, X.; Zhang, X.; Zhu, H.; Cheng, H. Novel gas sensing platform based on a stretchable laser-induced graphene pattern with self-heating capabilities. *J. Mater. Chem. A* **2020**, *8*, 6487.
(38) Huang, X.; Wu, P. A. Facile, High-Yield, and Freeze-and-Thaw-Assisted Approach to Fabricate MXene with Plentiful Wrinkles and Its Application in On-Chip Micro-Supercapacitors. *Adv. Funct. Mater.* **2020**, *30*, 1910048.
(39) Ghidiu, M.; Lukatskaya, M. R.; Zhao, M. Q.; Gogotsi, Y.; Barsoum, M. W. Conductive two-dimensional titanium carbide 'clay' with high volumetric capacitance. *Nature* **2014**, *516*, 78−81.
(40) Shi, X.; Wang, H.; Xie, X.; Xue, Q.; Zhang, J.; Kang, S.; Wang, C.; Liang, J.; Chen, Y. Bioinspired Ultrasensitive and Stretchable MXene-Based Strain Sensor via Nacre-Mimetic Microscale "Brick-and-Mortar" Architecture. *ACS Nano* **2019**, *13*, 649−659.
(41) Vecchio, D. A.; Mahler, S.; Hammig, M. D.; Kotov, N. A. Structural Analysis of Nanoscale Network Materials Using Graph Theory. *ACS Nano* **2021**, *15*, 12847.
(42) Vecchio, D. A.; Hammig, M. D.; Xiao, X.; Saha, A.; Bogdan, P.; Kotov, N. A. Spanning Network Gels from Nanoparticles and Graph Theoretical Analysis of Their Structure and Properties. *Adv. Mater.* **2022**, *34*, 2201313.
(43) Gutmana, I.; Körtvélyesi, T. Wiener Indices and Molecular Surfaces. *Z. Naturforsch., A: Phys. Sci.* **1995**, *50*, 669−671.
(44) Li, Q.; Xu, X.; Guo, J.; Hill, J. P.; Xu, H.; Xiang, L.; Li, C.; Yamauchi, Y.; Mai, Y. Two-Dimensional MXene-Polymer Heterostructure with Ordered In-Plane Mesochannels for High-Performance Capacitive Deionization. *Angew. Chem., Int. Ed.* **2021**, *60*, 26528−26534.
(45) Zangmeister, R. A.; Morris, T. A.; Tarlov, M. J. Characterization of Polydopamine Thin Films Deposited at Short Times by Autoxidation of Dopamine. *Langmuir* **2013**, *29*, 8619−8628.
(46) Wang, Z.; Zou, Y.; Li, Y.; Cheng, Y. Metal-Containing Polydopamine Nanomaterials: Catalysis, Energy, and Theranostics. *Small* **2020**, *16*, 1907042.
(47) Jiang, Y.; Pan, X.; Yao, M.; Han, L.; Zhang, X.; Jia, Z.; Weng, J.; Chen, W.; Fang, L.; Wang, X.; Zhang, Y.; Duan, R.; Ren, F.; Wang, K.; Chen, X.; Lu, X. Bioinspired adhesive and tumor microenvironment responsive nanoMOFs assembled 3D-printed scaffold for anti-tumor therapy and bone regeneration. *Nano Today* **2021**, *39*, 101182.
(48) Li, Z.; Paul, R.; Tis, T. B.; Saville, A. C.; Hansel, J. C.; Yu, T.; Ristaino, J. B.; Wei, Q. Non-invasive plant disease diagnostics enabled by smartphone-based fingerprinting of leaf volatiles. *Nat. Plants* **2019**, *5*, 856−866.
(49) Broza, Y. Y.; Mochalski, P.; Ruzsanyi, V.; Amann, A.; Haick, H. Hybrid Volatolomics and Disease Detection. *Angew. Chem., Int. Ed.* **2015**, *54*, 11036−11048.
(50) Broza, Y. Y.; Zhou, X.; Yuan, M.; Qu, D.; Zheng, Y.; Vishinkin, R.; Khatib, M.; Wu, W.; Haick, H. Disease Detection with Molecular Biomarkers: From Chemistry of Body Fluids to Nature-Inspired Chemical Sensors. *Chem. Rev.* **2019**, *119*, 11761−11817.
(51) Mills, G. A.; Walker, V. Headspace solid-phase microextraction profiling of volatile compounds in urine: application to metabolic investigations. *J. Chromatogr. B* **2001**, *753*, 259−268.
(52) De Lacy Costello, B.; Amann, A.; Al-Kateb, H.; Flynn, C.; Filipiak, W.; Khalid, T.; Osborne, D.; Ratcliffe, N. M. A review of the volatiles from the healthy human body. *J. Breath Res.* **2014**, *8*, 014001.
(53) Broza, Y. Y.; Vishinkin, R.; Barash, O.; Nakhleh, M. K.; Haick, H. Synergy between nanomaterials and volatile organic compounds for non-invasive medical evaluation. *Chem. Soc. Rev.* **2018**, *47*, 4781.
(54) Stavropoulos, G.; van Munster, K.; Ferrandino, G.; Sauca, M.; Ponsioen, C.; van Schooten, F.-J.; Smolinska, A. Liver Impairment—The Potential Application of Volatile Organic Compounds in Hepatology. *Metabolites* **2021**, *11*, 618.
(55) Jian, Y.; Zhang, N.; Liu, T.; Zhu, Y.; Wang, D.; Dong, H.; Guo, L.; Qu, D.; Jiang, X.; Du, T.; Zheng, Y.; Yuan, M.; Fu, X.; Liu, J.; Dou, W.; Niu, F.; Ning, R.; Zhang, G.; Fan, J.; Haick, H.; Wu, W. Artificially Intelligent Olfaction for Fast and Noninvasive Diagnosis of Bladder Cancer from Urine. *ACS Sens* **2022**, *7*, 1720−1731.
(56) Jin, H.; Yu, J.; Lin, S.; Gao, S.; Yang, H.; Haick, H.; Hua, C.; Deng, S.; Yang, T.; Liu, Y.; Shen, W.; Zhang, X.; Zhang, X.; Shan, S.; Ren, T.; Wang, L.; Cheung, W.; Kam, W.; Miao, J.; Chen, D.; Cui, D. Nanosensor-Based Flexible Electronic Assisted with Light Fidelity Communicating Technology for Volatolomics-Based Telemedicine. *ACS Nano* **2020**, *14*, 15517−15532.

https://doi.org/10.1021/acsnano.2c08266
ACS Nano 2022, 16, 17376−17388

(57) Khatib, M.; Haick, H. Sensors for Volatile Organic Compounds. *ACS Nano* **2022**, *16*, 7080−7115.
(58) Jurs, P. C.; Bakken, G. A.; McClelland, H. E. Computational Methods for the Analysis of Chemical Sensor Array Data from Volatile Analytes. *Chem. Rev.* **2000**, *100*, 2649−2678.
(59) Laurens, V. D. M.; Hinton, G. Visualizing Data using t-SNE. *J. Mach. Learn. Res.* **2008**, *9*, 2579−2605.
(60) Shehada, N.; Cancilla, J. C.; Torrecilla, J. S.; Pariente, E. S.; Bronstrup, G.; Christiansen, S.; Johnson, D. W.; Leja, M.; Davies, M. P.; Liran, O.; Peled, N.; Haick, H. Silicon Nanowire Sensors Enable Diagnosis of Patients via Exhaled Breath. *ACS Nano* **2016**, *10*, 7047−57.
(61) Wu, N.; Zhang, X. Y.; Xia, J.; Li, X.; Yang, T.; Wang, J. H. Ratiometric 3D DNA Machine Combined with Machine Learning Algorithm for Ultrasensitive and High-Precision Screening of Early Urinary Diseases. *ACS Nano* **2021**, *15*, 19522−19534.
(62) Tian, F.; Zhang, S.; Liu, C.; Han, Z.; Liu, Y.; Deng, J.; Li, Y.; Wu, X.; Cai, L.; Qin, L.; Chen, Q.; Yuan, Y.; Liu, Y.; Cong, Y.; Ding, B.; Jiang, Z.; Sun, J. Protein analysis of extracellular vesicles to monitor and predict therapeutic response in metastatic breast cancer. *Nat. Commun.* **2021**, *12*, 2536.

https://doi.org/10.1021/acsnano.2c08266
ACS Nano 2022, 16, 17376−17388